Journal of Materials Chemistry A

ROYAL SOCIETY OF CHEMISTRY

PAPER

View Article Online
View Journal | View Issue

Cite this: J. Mater. Chem. A, 2025, 13, 32539

Structural and electronic tunability of Ruddlesden–Popper oxyfluorides through nickel–copper substitution in $La_2Ni_{1-x}Cu_xO_{2.5}F_3$ ($0 \leq x \leq 1$)

Jonas Jacobs, *[a] Clemens Ritter,[b] Ke Xu,[c] Jörn Schmedt auf der Günne,[c] Hai-Chen Wang,[d] Miguel A. L. Marques,[d] Anja Hofmann,[e] Roland Marschall[e] and Stefan G. Ebbinghaus[a]

In this contribution we report on the synthesis, structure and optical characterization of Ruddlesden–Popper oxyfluorides $La_2Ni_{1-x}Cu_xO_{2.5}F_3$ ($0 \leq x \leq 1$) obtained by topochemical low-temperature fluorination of $La_2Ni_{1-x}Cu_xO_4$ with polyvinylidene fluoride (PVDF). Our study reveals that the anionic ordering in the tetragonal unit cell of $La_2NiO_{2.5}F_3$ persists even at high Cu substitution levels ($x = 0.9$), with minimal change in unit cell volume. This observation is contrary to expectations based on Jahn–Teller induced unit cell distortions, which were previously reported for the oxides $La_2Ni_{1-x}Cu_xO_4$, as well as for the closely related oxyfluorides $La_2Ni_{1-x}Cu_xO_3F_2$. The pure copper-containing compound $La_2CuO_{2.5}F_3$ crystallizes in a triclinic version of the same structure, and the symmetry lowering is attributed to the enhanced space requirements of the Jahn–Teller elongated CuO_4F_2 octahedra. The structural investigations based on XRD and ND Rietveld refinements are supported by low-field ^{19}F MAS NMR experiments. We also report the results of diffuse reflectance UV-Vis measurements, which are complemented by DFT calculations. Here, we demonstrate a strong impact of the Cu substitution on the electronic structure of the oxyfluorides, resulting in band gap energies in the range of 3.4 eV to 1.3 eV, spanning the whole visible spectrum. Notably, first photocatalytic water splitting tests reveal a considerable hydrogen evolution activity for $x = 0.2$, highlighting the potential of Ruddlesden–Popper oxyfluorides for solar energy applications.

Received 11th July 2025
Accepted 21st August 2025

DOI: 10.1039/d5ta05605e

rsc.li/materials-a

Introduction

Compounds with the Ruddlesden–Popper (RP) structure type $(AX)(ABX_3)_n$ (A, B are the cations and X are the anions) are a hot topic in solid state materials chemistry. The characteristic arrangement of ABX_3 perovskite layers with thickness n alternatingly interconnected with one halite AX layer results in a high structural flexibility, which gives rise to different electronic, magnetic, and optical properties. Therefore Ruddlesden–Popper compounds are interesting for both fundamental research and industrial applications, for example in the fields of energy storage,[1,2] catalysis,[3,4] and electronics.[5,6] Recently superconductivity was observed for the infinite 2D nickelates like $NdNiO_2$[7,8] and also for the bilayer $n = 2$ and trilayer $n = 3$ nickelates $La_3Ni_2O_7$ and $La_4Ni_3O_{10}$ when pressurized to 14 GPa[9] and 69 GPa[10] respectively.

An important part of the compositional flexibility of RP-compounds results from a high flexibility towards deviations from the ideal anion composition. In the case of $n = 1$ both over-stoichiometric[11] and under-stoichiometric[12] compounds are found. As a result, aliovalent anion substitution, for example, of one O^{2-} anion with two F^- anions can be used to obtain compounds with modified physical properties. Such fluorination reactions are for example possible by reacting oxide precursors with the fluorinated polymers polyvinylidene fluoride (PVDF, $[CH_2CF_2]_n$) or poly tetrafluoroethylene (PTFE, $[CF_2CF_2]_n$) in a non-oxidizing low temperature reaction[13] yielding the corresponding oxyfluorides. These fluorinations often show highly complex reaction mechanisms involving several less fluorinated intermediates.[14] The resulting oxyfluorides generally show different physical properties than the precursor oxides. Examples are the significantly increased antiferromagnetic transition temperature in $Sr_{3.5}La_{0.5}Fe_3O_{7.5}F_{2.6}$ from $T_N \approx 50$ K to $T_N > 450$ K,[15] and the increased optical

[a]Martin Luther University Halle-Wittenberg, Faculty of Natural Sciences II, Institute of Chemistry, Inorganic Chemistry, Kurt-Mothes-Straße 2, 06120, Halle, Germany. E-mail: jonas.jacobs@chemie.uni-halle.de

[b]Institut Laue Langevin, 71 Avenue des Martyrs, 38000 Grenoble, France

[c]University of Siegen, Faculty IV: School of Science and Technology, Department of Chemistry and Biology, Inorganic Materials Chemistry, Adolf-Reichwein-Str. 2, 57076, Siegen, Germany

[d]Research Center Future Energy Materials and Systems of the University Alliance Ruhr, Interdisciplinary Centre for Advanced Materials Simulation, Ruhr University Bochum, Universitätsstraße 150, 44801, Bochum, Germany

[e]University of Bayreuth, Department of Chemisty, Universitätsstraße 30, 95447 Bayreuth, Germany

band gaps (E_g) of 3.4 eV in the 3F-oxyfluoride $La_2NiO_{2.5}F_3$ [16] *vs.* 1.3 eV [17] for La_2NiO_4 which was obtained from UV-Vis measurements as well as band structure calculations making this compound of potential interest for applications using the high energy range of the solar spectrum. A similar change of E_g from 2.3 eV in $LaBaInO_4$ to 1.9 and 3.3 eV in $LaBaInO_3F_2$ was recently reported to result from topochemical fluorination.[18]

In our previous work on the substitution series $La_2Ni_{1-x}Cu_xO_3F_2$ ($0.0 \leq x \leq 1.0$) we reported a strong impact of the Ni/Cu ratio on the structural distortion (orthorhombic → monoclinic → triclinic, with increasing x)[19,20] which is linked to an increased Jahn–Teller distortion of the Ni/CuO_4F_2 octahedra. We also highlighted the resulting change in thermal stability (increase of the decomposition temperature from 460 °C for $x = 0.0$ and 420 °C for $x = 1.0$ up to 520 °C with $x = 0.6$)[21] as well as the tunability of the antiferromagnetic Néel temperature in the range of 40 K to 260 K.

In this study, we present the even higher fluorinated compounds of the substitution series $La_2Ni_{1-x}Cu_xO_{2.5}F_3$ with three F^- per formula unit over the complete range ($0.0 \leq x \leq 1.0$). The compounds are obtained by the topochemical low-temperature fluorination with PVDF as fluorination agent. Structural characterization using XRD and ND Rietveld refinements clarify the impact of the Ni/Cu ratio on the changes of the anion-ordered crystal structure. In addition, the Ni/Cu ratio results in strong changes in the optical band gaps which are analysed by UV-Vis measurements. Our results are complemented by DFT calculations and photocatalytic hydrogen evolution tests, which show a significant activity.

Experimental section

Synthesis

The precursor oxides of the $La_2Ni_{1-x}Cu_xO_4$ solid solution were synthesized in steps of $x = 0.1$ by a citric acid assisted combustion method as reported before.[19] In short, stoichiometric amounts of La_2O_3 (Merck) (dried at 900 °C for 10 h), Ni powder (Sigma-Aldrich) and copper(II) acetate (98%; Sigma-Aldrich) were dissolved in distilled water containing a few drops of concentrated HNO_3 and citric acid (molar ratio metal ions : citric acid = 1 : 3). The oxides were obtained by evaporating the water on a hot plate at 100 °C, carbonization of the resulting gel at 350 °C and subsequent calcination at 950 °C for 6 h in a box furnace in static air. The oxyfluorides $La_2Ni_{1-x}Cu_xO_{2.5}F_3$ were synthesized by mixing the oxides with polyvinylidene fluoride ($(PVDF/CH_2CF_2)_n$) (Alfa Aesar) in a molar ratio of 1 : 1.5 (oxide : CH_2CF_2) with a small excess of 2% polymer. The mixtures were slowly (2 °C min^{-1}) heated to 340 °C, kept at this temperature for 28 h and afterwards allowed to cool down to room temperature in the box furnace.

Characterization

X-ray diffraction (XRD) patterns were recorded on a Bruker AXS D8-Advance diffractometer operating in Bragg–Brentano geometry. Cu-K$\alpha_{1,2}$ radiation was used and the device was equipped with a 1D silicon strip detector (LYNXEYE). Patterns were recorded in the angular range $2\theta = 10$–$140°$ with a step size of 0.01° and a time of 3 s per step. Additionally, a STOE STADI MP diffractometer operating in transmission geometry with monochromatic Mo-Kα_1 radiation and equipped with a DECTRIS MYTHEN2 1 K detector was used to record patterns in the angular range of 2θ = 5–75° with a data point resolution of 0.015° and a total acquisition time of 2 h per scan.

Neutron powder diffraction (NPD) data of selected oxyfluorides (x = 0.3, 0.7, 0.9, 1.0) were collected on the high-resolution powder diffractometer D2B at the Institute Laue-Langevin in Grenoble, France. Beamtime was granted for proposal 5-23-769.[22] Measurements were performed at 300 K with λ = 1.594 Å for sample amounts of ~1.5 g (6 mm V-cylinder) and acquisition times of about 3 h per sample. For Rietveld refinements of XRD and NPD data GSAS II[23] was used.

The samples were checked for possible residual fluorination agent as well as other carbon related impurities by infrared spectroscopy on an ATR-FT-IR Bruker Tensor 27 spectrometer in the range 4000–250 cm^{-1}.

UV-Vis spectra were recorded in diffuse reflection mode on a PerkinElmer Lambda 19 spectrometer in praying mantis geometry in the range of $\lambda = 1350$–250 nm with 1 nm resolution. $BaSO_4$ (99.998%, Alfa Aesar) was used as white standard.

The La, Ni, and Cu contents of pelletized powder samples (10 wt% cellulose as binder) were quantified by X-ray fluorescence spectroscopy (XRF) using a Panalytical Epsilon 4 spectrometer. Data analysis was carried out based on the fundamental parameter approach (Omnian mode) based on 6 independent scans with excitation voltages between 5 and 50 kV in combination with filters of different materials and thicknesses (Ag, Cu, Al, and Ti).

Iodometric titration was used for the determination of the average Ni/Cu oxidation states. About 35 mg of the samples were dissolved in concentrated HCl containing an excess of KI. Afterward, 1 g of $NaHCO_3$ was added to adjust the pH and to create a CO_2 saturated atmosphere preventing the solutions from oxidation. For titration a 0.005 M $Na_2S_2O_3$ solution was used. The obtained oxidation state was calculated from three averaged titrations per sample.

^{19}F Magic Angle Spinning (MAS) NMR experiments were performed on a 1.4 T magnet in combination with an Avance II Bruker NMR console running Topspin V2.1, operating at a frequency of 56.4 MHz. Magic angle sample spinning on the 1.4 T magnet was carried out with a home-made conical stator with the sample packed in 3D printed conical rotors, spinning at approximately 19 kHz.[24] The chemical shift values refer to $CFCl_3$, according to the IUPAC list of reference compounds.[25] The spectra were analyzed with deconv2Dxy.[26] The repetition delay was set as 1 s.

Photocatalytic hydrogen evolution experiments were performed for selected oxyfluorides with x = 0.0, 0.2, and 0.4. 75 mg of the samples were dispersed in 150 mL of ultrapure water with TOC = 2 ppb containing 10% ethanol. The dispersion was continuously stirred at of 20 °C (Lauda thermostat (ECO RE1050G)). The reactor was flushed with Argon (grade 5.0, purity ≥ 99.999%) with a flow rate of 100 mL min^{-1} (Bronkhorst mass flow controller) to remove all residues of air. Afterwards,

the flow rate was reduced to 25 mL min^{-1} of Argon and the online detection of the evolved gases was performed using a GC2014 gas chromatograph from Shimadzu, equipped with a shin carbon ST column (Restek) and a thermal conductivity detector, using Argon as carrier gas. Dark measurements were performed before starting the irradiation of the sample with a 300 W Xe lamp (Quantum Design) for 2.0 to 2.5 h. Then the lamp was turned off and the evolved gases were detected until a reduced hydrogen evolution was detected. Afterwards, an H_2PtCl_6 solution was added through a rubber sealing without opening the reactor to reach a concentration of 0.5 wt% of Pt. Then, the lamp was turned on again and the sample was irradiated for another 2 h. The lamp was turned off and the detection of the evolved gasses was performed until no hydrogen could be detected anymore. For comparison, a 10% aqueous ethanol solution was also measured without the addition of a sample. The ethanol solution was irradiated for 3.5 h with the same 300 W Xe lamp. Afterwards, the gas evolution was detected until no gas was evolved anymore.

Density functional theory (DFT) calculations were performed within the projector augmented wave (PAW) formalism,[27] as implemented in the Vienna *ab initio* simulation package (VASP).[28,29] A plane-wave basis cutoff of 520 eV was set and total energy convergence was ensured to be within 0.01 meV per unit cell. For geometry optimization, the Perdew–Burke–Ernzerhof exchange–correlation functional for solids (PBEsol)[30] was applied and the Γ-centered k-point grids with a density of 2000 k-points per reciprocal atom (kppa) were used to sample the Brillouin zone. An effective on-site Coulomb correction[31] of 6.2 eV was applied for Ni 3d states and denser (4000 kppa) k-grids were used to obtain the electronic structures. For compositions containing both Ni and Cu various magnetic and structural configurations were generated using the cluster expansion method implemented in the ATAT package.[32] To simulate the behavior of disordered Ni/Cu occupations, the band gaps were averaged for multiple ordered configurations with weights according to the Boltzmann distribution of their total energies, using the generalized quasichemical approximation (GQCA).[33,34] Furthermore, the band structure of the mixed cationic configuration with the largest gap at $x = 0.25$ (75% Ni ratio) was un-folded into the pure $La_2NiO_{2.5}F_3$ Brillouin zone using the Python package Easyunfold.[35]

Results and discussion

Structure and composition of oxyfluorides $La_2Ni_{1-x}Cu_xO_{2.5}F_3$

Based on the results of our previous work on $La_2NiO_{2.5}F_3$ the oxyfluorides are best prepared by topochemical fluorination of oxides obtained from soft chemistry synthesis. In contrast, fluorination of solid state precursors usually results in partial decomposition of the desired oxyfluoride before complete formation.[16] More reactive soft chemistry precursor oxides were therefore prepared by a citrate-based approach. These precursor oxides were also used for the closely related oxyfluorides $La_2Ni_{1-x}Cu_xO_3F_2$ which we reported previously.[19,21] For the $x = 0$ compound ($La_2NiO_{2.5}F_3$) a pronounced metastability was found in previous *in situ* XRD experiments.[14,16] Preliminary temperature-dependent *in situ* XRD experiments were therefore used to establish suitable reaction conditions for the samples in this work. Based on these investigations bulk synthesis was performed at 340 °C for 28 h. Such reaction optimization experiments were especially needed for the Cu-rich compounds of the substitution series as the stability of the oxyfluorides was found to further decrease with increasing Cu substitution level. All oxyfluorides with the formula $La_2Ni_{1-x}Cu_xO_{2.5}F_3$ were obtained phase pure in the full range of $0 \leq x \leq 1$ applying these conditions. The absence of significant amounts of unreacted PVDF as well as other residual organic compounds in the final products was routinely checked by IR spectroscopy (not shown) and later confirmed by ^{19}F MAS NMR spectroscopy (*vide infra*) for the sample with $x = 0.0$, 0.3, and 0.7. Only for the $x = 1$ sample a weak PVDF signal was found most probably resulting from the slight excess of PVDF which was used for the synthesis. The La : Ni : Cu ratio of the resulting products was determined *via* XRF spectroscopy and no major deviations from the expected value of $La : (Ni_{1-x}Cu_x) = 2 : 1$ was found as the ratios were ranging from 1.9 to 2.1. Additionally, for the Ni : Cu ratio no considerable deviations from the nominal x values were observed either. The fluorination with PVDF is expected to be non-oxidative[36] and therefore no deviations of the oxidation state of nickel/copper from +2 is expected. This assumption was checked for two selected samples ($x = 0.3$, and 0.7) by iodometric titration and average oxidation states of +2 (2.07(2), and 2.02(2)) was found for the B-type cations for both samples. This finding is in good agreement with the results of iodometric titrations, which we previously performed for the starting oxides as well as members of the 2F-substitution series $La_2Ni_{1-x}Cu_xO_3F_2$, where also no hints for a change of the oxidation states was found.[19] An average oxidation state of +2 and fully occupied anion sites derived from neutron powder diffraction (*vide infra*) were seen as confirmation of the nominal $O_{2.5}F_3$ anion stoichiometry. This is in agreement with the results obtained with an F^- ion sensitive electrode that were previously performed for the $x = 0.0$ compound $La_2NiO_{2.5}F_3$.[16]

The XRD patterns of all oxyfluorides $La_2Ni_{1-x}Cu_xO_{2.5}F_3$ are shown in Fig. 1. Only subtle changes in the reflection positions are observed for all compounds with $0 \leq x \leq 0.9$ and the diffraction patterns qualitatively resemble the one of $La_2NiO_{2.5}F_3$. This observation is highly surprising as both the starting oxides and the 2F-oxyfluorides were previously found to exhibit prominent Ni/Cu-dependent unit cell distortions with a corresponding symmetry lowering from tetragonal to orthorhombic for the oxides ($I4/mmm \rightarrow Bmab$)[37] and orthorhombic to monoclinic to triclinic for the oxyfluorides ($Cccm \rightarrow C2/c \rightarrow P\bar{1}$).[19] This symmetry lowering is the result of an increased space requirement of the BX_6 octahedra caused by Jahn–Teller elongation due to introduction of Cu^{2+} with d^9 electron configuration. In the case of the here investigated oxyfluorides a deviating diffraction pattern is only observed for $x = 1$ where clear shoulders appear at both sides of the (113) peak (indexed and marked with arrows in Fig. 1). These shoulders in combination with a further splitting of several other reflections indicate a symmetry lowering to triclinic. A triclinic unit cell metric was also obtained for the corresponding 2F-oxyfluoride

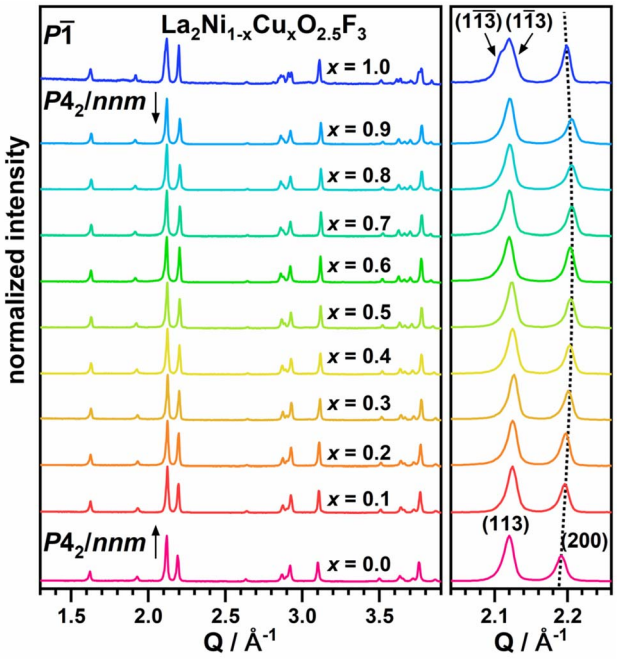

Fig. 1 XRD patterns of all members of the solid solution $La_2Ni_{1-x}Cu_xO_{2.5}F_3$ and a detailed view of the (113) and (200) main reflections. The shift of (200) is highlighted by a slightly curved, dotted line as guide for the eye. For $x = 1$ indices are given for two of the additional reflections resulting from the triclinic unit cell symmetry.

$La_2CuO_3F_2$.[20] It has to be noted though that both compounds ($La_2CuO_3F_2$ and $La_2CuO_{2.5}F_3$) exhibit clearly different diffraction patterns resulting from different structural distortions.

Rietveld refinements were conducted for all oxyfluorides in order to quantify the Ni/Cu-dependent changes in the unit cell parameters as well as to confirm the structural distortions. These refinements were performed as joint refinements based on two independent X-ray datasets (Cu-K$\alpha_{1,2}$, and Mo-Kα_1 radiation). By this approach we were able to achieve higher data redundancy combining the advantages of the increased angular resolution of the Cu-K$\alpha_{1,2}$ patterns with the higher accessible Q-range in the transmission Mo-Kα_1 data. For selected substitution levels ($x = 0.3$, 0.7, and 0.9) neutron powder diffraction patterns were additionally combined with the XRD data. Both XRD patterns were given the weighting factor 0.5 and the NPD data got the weighting factor 1 in the refinements. The Rietveld plots for the X-ray and neutron diffraction patterns of $x = 0.3$ and 0.7 are shown in Fig. 2. Rietveld plots of all other refinements and the obtained crystallographic parameters can be found in the supplement (Fig. S1, S2, Tables S1 and S3). Due to the high structural similarity the assignment of the anions to the different positions was performed according to the pure nickel compound ($La_2NiO_{2.5}F_3$). Here based on DFT and BVS calculations oxygen was found to be located on the equatorial octahedral positions (O_{eq1}; 4*d*, and O_{eq2}; 4*g*) as well as one interstitial position (O_{int}; 2*b*) and fluorine is located on the apical octahedral positions (F_{ap}; 8*m*) as well as on one interstitial site (F_{int}; 4*c*) giving an overall $\frac{3}{4}$ interstitial anion occupation.[16]

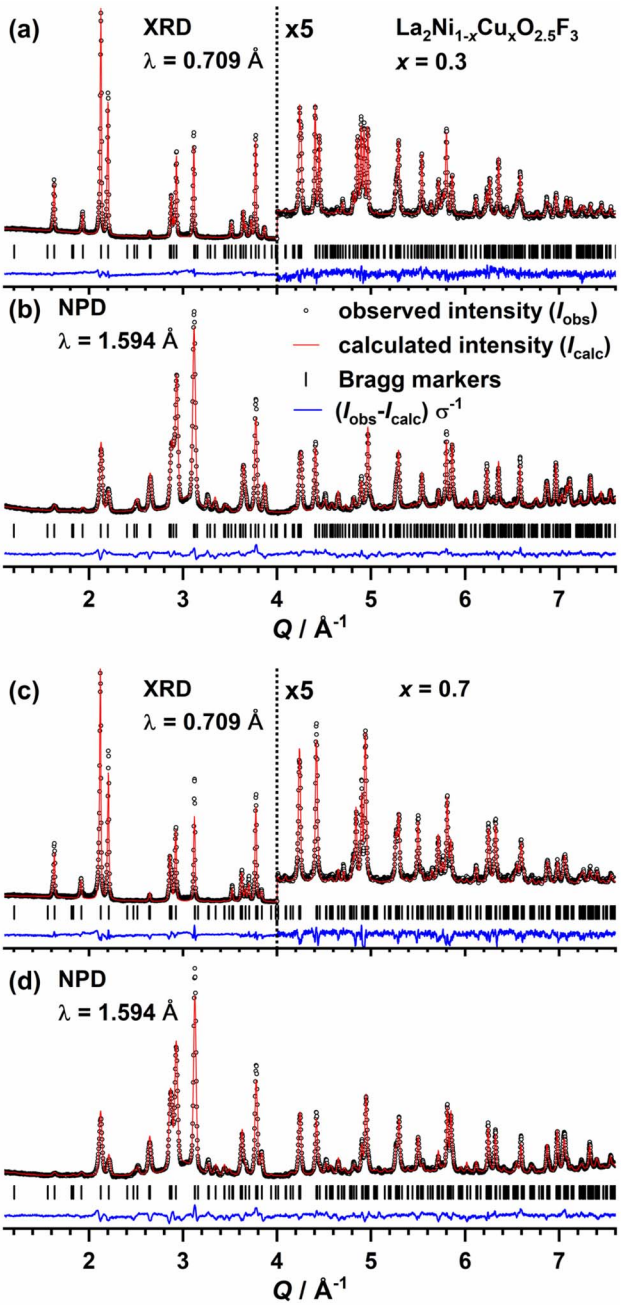

Fig. 2 Rietveld plots obtained for the joint refinements of X-ray and neutron powder diffraction data of $La_2Ni_{0.7}Cu_{0.3}O_3F_2$ (a and b) and $La_2Ni_{0.3}Cu_{0.7}O_3F_2$ (c and d). Refinements were carried out using the structure model of $La_2NiO_{2.5}F_3$ ($P4_2/nnm$).

From the difference Fourier map obtained for the NPD data missing scattering density was found to be located near the apical anion positions for both $x = 0.3$ and 0.7. A similar observation was previously made for the neutron diffraction data of the 2F-oxyfluoride $La_2Ni_{0.2}Cu_{0.8}O_3F_2$ for which a split apical position (F_{ap}) due to local occurrence of Jahn–Teller elongated CuO_4F_2 and non-elongated NiO_4F_2 octahedra was derived.[20] Final refinements of the $x = 0.3$ and 0.7 datasets of this work were therefore performed in the $La_2NiO_{2.5}F_3$ structure

model including a split apical (8*m*) anion position (denoted as F_{ap1}, and F_{ap2}). With this structure model good fits were obtained for all datasets and two different inter atomic distances are obtained for the apical octahedral positions ($x = 0.3$: Ni/Cu–F_{ap1} = 2.15 Å and Ni/Cu–F_{ap2} = 2.37 Å, $x = 0.7$: Ni/Cu–F_{ap1} = 2.07 Å and Ni/Cu–F_{ap2} = 2.36 Å) indicative of the Jahn–Teller stretching of the CuO_4F_2 octahedra. These distances are close to the ones observed for $La_2Ni_{0.2}Cu_{0.8}O_3F_2$ (Ni/Cu–F_{ap} = 2.09 Å and 2.30 Å).[20] The refinement of fractional site occupation factors (*sof*) (assuming a complete total occupation as found in initial refinement runs) gave values of $sof_{Fap1}/sof_{Fap2} \approx 0.7/0.3$ for $x = 0.3$ and 0.3/0.7 for $x = 0.7$ resembling the nominal Ni/Cu values. The good agreement of the occupation factors with the atomic distances is a clear confirmation that the different octahedral geometries indeed result from the Jahn–Teller distortion of the Cu^{2+}-environment and that the shorter distance reflects the Ni–F_{ap1} bond while the longer distance corresponds to the Cu–F_{ap2} bond. The refined unit cell of $x = 0.3$ and a detailed view of one (Ni,Cu)O_4F_2 octahedron (for $x = 0.3$) is shown in Fig. 3. The structure of $x = 0.7$ is highly similar and therefore not shown here.

In addition to the increased Cu–F_{ap2} distance, the CuO_4F_2 octahedron exhibits a significantly increased octahedral tilt compared to the NiO_4F_2 octahedron. Interestingly, no indications for a splitting for the equatorial position (O_{eq2}; 4*g*) were observed. This results in stronger deviations of the F_{ap}–Ni/Cu–O_{eq2} angle from the expected 90° angle, *i.e.* ∠(F_{ap1}–Ni/Cu–O_{eq2}) ~88° and ∠(F_{ap2}–Ni/Cu–O_{eq2}) ~80° for both Ni/Cu ratios. A possible explanation is the contraction of the equatorial plane associated with the Jahn–Teller stretching, which is opposed to a further deflection of the equatorial position (4*g*) along *c*.

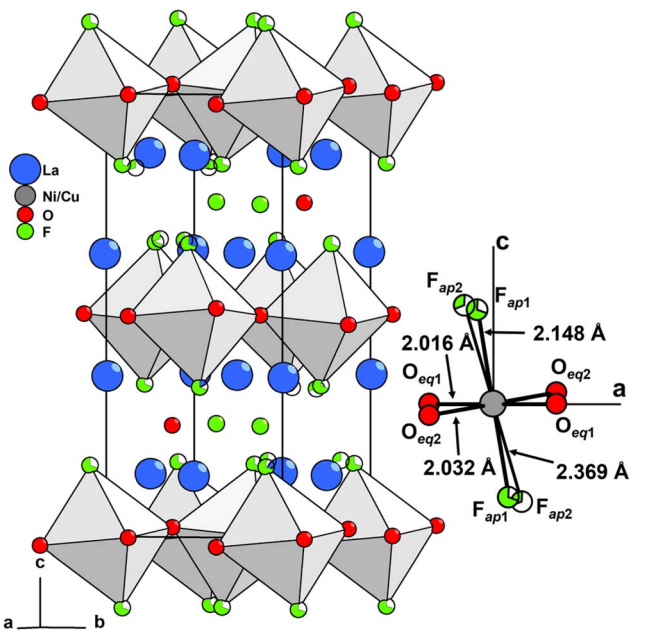

Fig. 3 The crystal structure of $La_2Ni_{1-x}Cu_xO_{2.5}F_3$ ($x = 0.3$) obtained from Rietveld refinements. An enlarged view of one Ni/CuO_4F_2 octahedron is additionally shown highlighting the different atomic distances and tilting directions.

Structure refinements with the same tetragonal structure model gave good fits for the X-ray diffraction data of all other compounds with $x = 0.0$ to 0.9. No additional unindexed or systematically extinct peaks, which would point to a different unit cell symmetry, were observed. The split apical position of $x = 0.3$ and 0.7 was not taken into account in these refinements as the anionic positions are subjected to an increased error in the presence of heavy scatterers like La, Ni, and Cu. The tetragonal structure of the pure nickel compound $La_2NiO_{2.5}F_3$ can therefore be confirmed to exist throughout the entire substitution series (except for $x = 1$; *vide infra*). The absence of structural transitions shows that the 3F structure has a significantly higher tolerance for additional octahedral stretching than the structural variant of the 2F oxyfluorides, where a symmetry reduction from orthorhombic (*Cccm*) to monoclinic (*C*2/*c*) symmetry already occurs at $x = 0.2$ due to the need of an additional tilting component of the octahedra.[19]

The unit cell parameters and selected atomic distances, which were obtained from the refinements, are shown in Fig. 4 for $x = 0.0$ to 0.9. For the cell parameters *a* and *c* a non-linear dependence on the Cu substitution level is apparent. The substitution series therefore does not follow Vegard's law. While parameter *a* decreases monotonously with *x*, *c* exhibits a non-monotonous dependency, with a minimum at $x = 0.1$–0.2 and a maximum at $x = 0.8$. The difference between these two extrema is 0.124 Å. This corresponds to only about 1/3 of the overall change in the long axis (0.370 Å) of the corresponding 2F oxyfluorides.[19] The deviation from the expected linear trend of *a*, and *c* might hint to a phase transition that is not resolved by the powder diffraction data. The assumption is in concordance with changes in the NMR spectra of the $x = 0.7$ sample (*vide infra*). To check for a possible phase transition, additional refinements in the five tetragonal translationengleiche sub groups of $P4_2/nnm$ ($P\bar{4}n2$, $P\bar{4}2m$, $P4_2nm$, $P4_222$, and $P4_2/n$) were carried out for the $x = 0.3$, and 0.7 datasets. None of these structure models resulted in a significant decrease of the quality factors R_w or χ^2 despite the higher number of refinable parameters. We therefore stick to the $P4_2/nnm$ structure model as correct choice for all compounds with $x \leq 0.9$. The non-monotonous cell parameter dependence on *x* also affects the unit cell volume. With increasing Cu content there is first a volume contraction up to $x = 0.3$, followed by a volume expansion reaching a maximum at $x = 0.6$, which is then followed by another volume contraction. The relative volume change compared to $La_2NiO_{2.5}F_3$ is slightly negative with the strongest change of −0.9% observed for $x = 0.3$. This finding is a serious difference to the 2F oxyfluorides $La_2Ni_{1-x}Cu_xO_3F_2$, in which Ni/Cu substitution leads to an almost linear enlargement of the unit cell of ~5%. The apical Ni/Cu-F_{ap} atomic distance (shown in Fig. 4d) clearly increases with the Cu content, which is expected due to the Jahn–Teller elongation. For the equatorial distances, a decrease is found for increasing *x*, which is in concordance with the expectations from the Jahn–Teller distortion. In principle, a corresponding increase in *c* would also be expected. However, the elongation of the copper-containing octahedra is compensated by a stronger tilting along [110] as described above for $x = 0.3$ and 0.7.

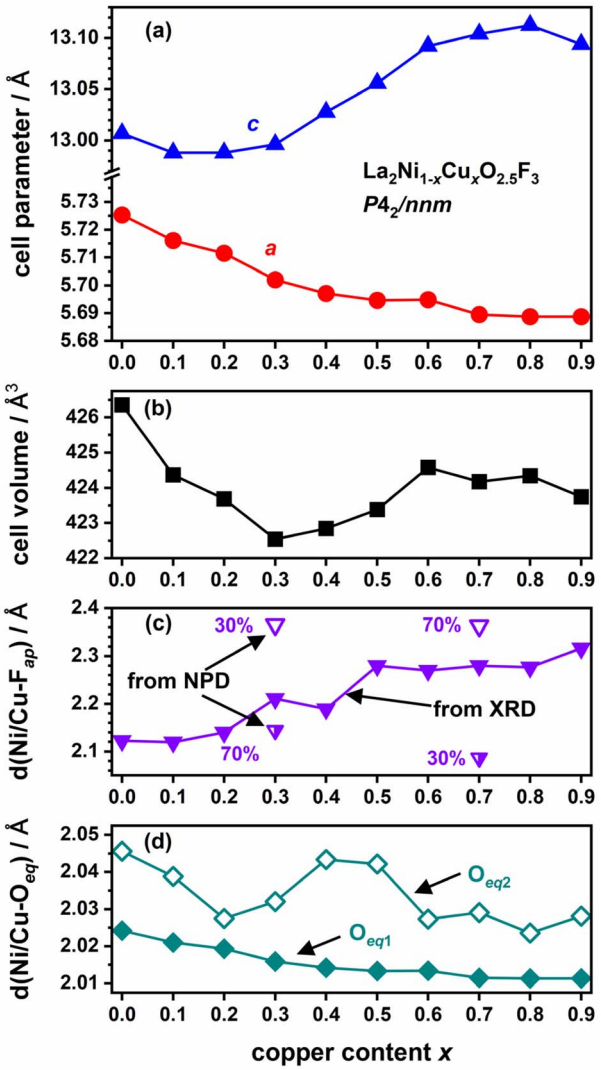

Fig. 4 Evolution of the unit cell parameters *a*, and *c* (a) and cell volume (b) as well as the apical (Ni/Cu−F_{ap}) and equatorial (Ni/Cu−O_{eq}) distances (c and d) with the copper content (*x*) as obtained by Rietveld refinements. The lines serve as guides to the eye. Error bars are not given as they are in the range of the symbol size.

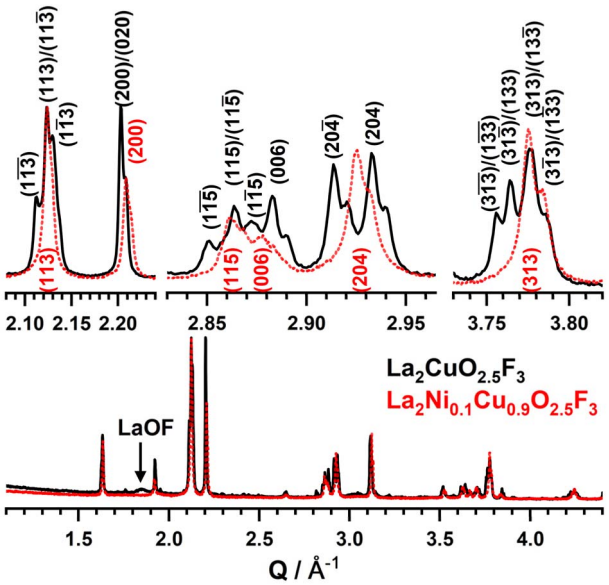

Fig. 5 Comparison of selected regions of the X-ray diffraction patterns of $x = 0.9$ and $x = 1.0$ obtained with Cu-K$\alpha_{1,2}$ radiation. Selected peaks are indexed highlighting the transition from tetragonal to triclinic.

Refinements of the $x = 1.0$ oxyfluoride $La_2CuO_{2.5}F_3$ were not successful when applying the tetragonal structure model due to the presence of additional diffraction peaks. Indexing these peaks in the XRD data can be performed in comparison to the $x = 0.9$ dataset as depicted in Fig. 5. Using the (113) main signal of the tetragonal structure, for example, it becomes clear that the observed splitting of the signal is not explained by a monoclinic unit cell symmetry, which would result in two signals for (113) and ($\bar{1}$13). The observation of a more complex splitting in at least three signals is the sign of a triclinic unit cell giving rise to (1$\bar{1}\bar{3}$) and (11$\bar{3}$). This interpretation is further supported by the splitting of the (204) peak into (20$\bar{4}$) and (204), which is also shown in the figure. An analogous splitting into (204) and (024) would have to be linked to clearly different values for *a* and *b*, which would, for example, give rise to a clear splitting of the (200) signal. However, this peak is not split, which is why a triclinic distorted version of the $P4_2/nnm$ unit cell with $a \approx b$ is most likely. Full profile fits with the LeBail method were used to extract the unit cell parameters from the XRD data ($P\bar{1}$, $a = b = 5.7079(1)$ Å, $c = 13.0818(2)$ Å, $\alpha = 89.65(1)°$, $\beta = 89.59(1)°$, $\gamma = 89.92(3)°$).

Structure refinements of $La_2CuO_{2.5}F_3$ were carried out with this triclinic unit cell. The refinements were performed as joint refinements against one XRD and NPD dataset. The structure model in space group $P\bar{1}$ was set up in the coordinate system of the tetragonal unit cell of the 3F-oxyfluorides and the Rietveld plots are shown in Fig. 6. The anionic positions were taken from the positions found in the CuO_4F_2 octahedra of the tetragonal structure model for $x = 0.9$. A good fit to the XRD data is obtained indicating a correct structure model with reliable cation positions (the structural parameters are given in Table S2 in the SI). In the NPD data some unmatched intensity is clearly visible. A reasonable fit to the NPD data can be obtained when freely refining the anion positions but this results in unreasonably strongly distorted CuO_4F_2 octahedra most probably due to too many refinable variables. For this reason, we do not report the results of this refinement here. Additionally, by closely inspecting the XRD data, some mismatched reflections of low intensity can be found at 0.81, 1.72, 1.76 $Å^{-1}$ and 1.95 $Å^{-1}$ of which the later three are marked with asterisks in the inset of Fig. 6a. These peaks cannot be described in the current structure model or be assigned to any previously known impurity phase. The same peaks are also present in different $La_2CuO_{2.5}F_3$ sample batches and might hint to an even more complex supercell arising from anion ordering. The full structure description of this compound will be addressed in a future article with the aid of high resolution/high intensity synchrotron XRD data, as well as high intensity, lower *Q* NPD data.

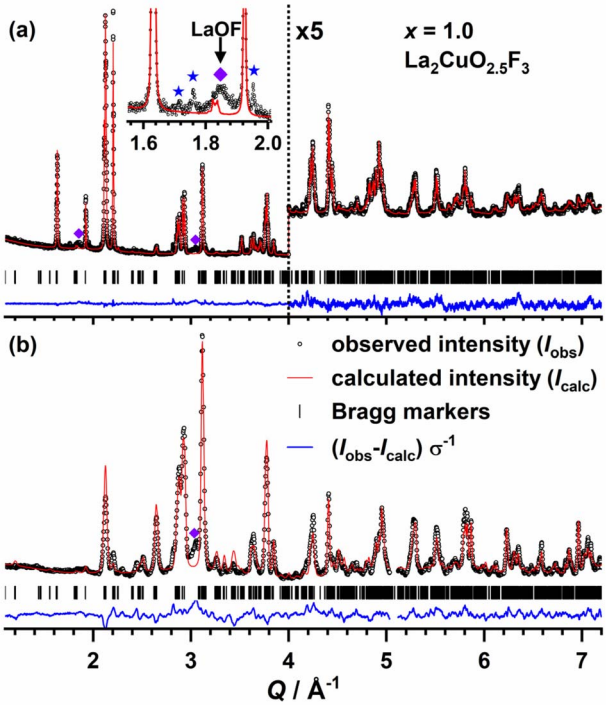

Fig. 6 Rietveld plots obtained for the refinement of $La_2CuO_{2.5}F_3$ in space group $P\bar{1}$ based on X-ray (a) and neutron (b) powder diffraction data. The position of LaOF signals is highlighted by violet diamonds. Asterisks highlight the additional reflections which were not indexable.

^{19}F MAS NMR experiments were performed to further study the fluorine environment for four selected compounds ($x = 0.0$, 0.3, 0.7, and 1.0), and the ^{19}F MAS NMR spectra are shown in Fig. 7. Spinning sidebands are successfully suppressed by the choice of a low field magnet (1.4 T) in combination with the high sample spinning frequency (~20 kHz). The repetition delay of 1 s was sufficiently long so that the fluorine atoms in the diamagnetic environments can also be measured quantitatively. The broadening caused by hyperfine interactions, dipolar coupling to Cu and F atoms nevertheless limits the resolution of the spectra. Based on the broadness of the peaks, all are found to originate from paramagnetic fluorine environments. One exception is the signal at −89 ppm that is assigned to unreacted PVDF (the spectrum of pure PVDF is additionally included) and its amount has to be below the detection limit of the IR-spectrometer used. The observation of two signals for $x = 0.0$, 0.3 and 1.0 points to the presence of two different fluorine environments, which is in good agreement with the expectations stemming from the structural refinements, as two different F-sites (namely: apical octahedral ($8m$) and interstitial sites ($4c$)) were derived for $La_2NiO_{2.5}F_3$ from BVS calculations.[16] The presence of two signals in similar intensity ratios between the compounds is therefore seen as confirmation of the proposed structural similarity of all oxyfluorides including the $x = 1.0$ compound. The observation of only one signal for $x = 0.7$ is counter intuitive as the same two anion sites are expected due to the strong structural similarity. A possible explanation is a change in the crystal symmetry, which is in agreement with the nonlinear change in the unit cell parameters (*vide supra*) and can't be ruled out based on the here discussed powder diffraction data.

The observed chemical shifts differ for all compositions and for the most intense peak values in the range of $\delta = -20$ ppm to 15 ppm are obtained without a clear correlation with the Cu content. The chemical shifts of the second signal are in the range of 89 ppm to 98 ppm. Differing chemical shifts were also observed for the ^{19}F MAS NMR spectra obtained for the 2F oxyfluorides $La_2Ni_{1-x}Cu_xO_3F_2$ and a possible explanation was seen in the changing La–F interactions due to changes in the F-environment caused by the Jahn–Teller elongation.[19] The same explanation holds for the spectra shown here. In addition, changes in the hyperfine shift, which is related to the distance and orientation of the paramagnetic centers Ni/Cu to F will also add to the different chemical shift values. It is interesting to note that the isotropic peaks of the 3F oxyfluorides presented here are clearly shifted to higher resonance frequencies compared to the 2F oxyfluorides for which δ-values in the region of −44 ppm were found.[19] This highlights the clear presence of different fluorine environments for both substitution series which is expected hence their different crystal structures. For example, in $La_2NiO_{2.5}F_3$ decreased F_{ap}–F_{ap} distances of neighboring octahedra compared to the 2F-oxyfluroides ($d(F_{ap}–F_{ap}) \approx$ 2.88 Å *vs.* 2.77 Å $La_2NiO_3F_2$ *vs.* $La_2NiO_{2.5}F_3$ respectively) are accompanied by additional F_{ap}–F_{int} interactions over a distance of 2.43 Å.

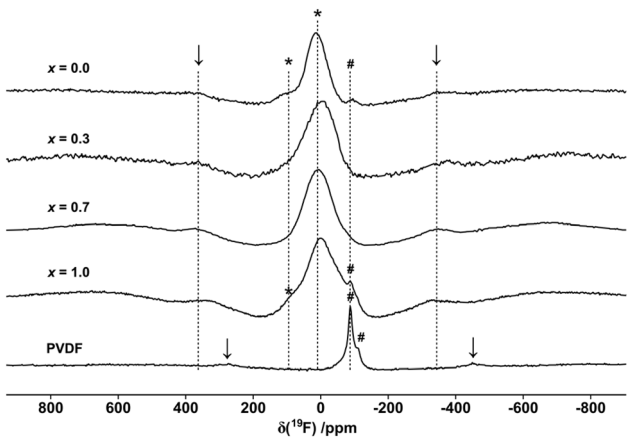

Fig. 7 ^{19}F MAS NMR spectra of $La_2Ni_{1-x}Cu_xO_3F_2$ with $x = 0.0$, $x = 0.3$, $x = 0.7$, $x = 1.0$, and PVDF. The samples were spinning at ≈ 20 kHz in a 1.4 T magnetic field. The dashed lines serve as guides to the eyes. The asterisks and hashes denote isotropic peaks.

Optical band gap determination and photocatalytic hydrogen evolution

In our previous study, it was shown that $La_2NiO_{2.5}F_3$ has an optical band gap of 3.4 eV [16] which is unusually large compared to the oxide and the 2F oxyfluoride $La_2NiO_3F_2$ (both appear black to the eye; La_2NiO_4 $E_g = 1.3$ eV [17]). The influence of Ni/Cu substitution on the optical properties of the oxyfluorides was studied by UV-Vis spectroscopy as well as DFT calculations.

Diffuse reflectance UV-Vis spectra were obtained in order to quantify the changes in the optical band gap energy. These spectra consist of several features for the compounds in the range of $x = 0$–0.6, which indicate different transitions in the band gap region (compare Fig. 8a). Tauc plots of the data converted by the Kubelka–Munk function with exponents of $\frac{1}{2}$ (indirect transition) and 2 (direct transition) were used to determine the band gap energy of these transitions.[38] These plots are shown in the supplement (Fig. S3) for $x = 0.4$ as example. The use of the exponent $n = \frac{1}{2}$ allows the determination of E_g for all observed features *e.g.* band transitions, while the feature at higher energies is strongly favoured if a direct transition ($n = 2$) is assumed. This is why the $n = \frac{1}{2}$ exponent seems more reasonable which is also in concordance with the initial reported data of $La_2NiO_{2.5}F_3$. The band gap energies (shown in Fig. 8b) were nevertheless determined for all compounds applying both exponents. For $n = 2$, only one transition could be reasonably analysed in each case and, compared to $n = \frac{1}{2}$, larger values of E_g are determined. Based on the visual impression of the samples with $x = 0.0$ to 0.6 which are shown in Fig. 9. It can be seen that the change in E_g is accompanied by a change in the colour of the oxyfluoride powder ranging from greyish white ($x = 0$) *via* ochre to reddish brown for $x = 0.5$ (E_g: 1.93/1.31 eV with $n = 1/2$). Starting from $x \geq 0.6$, the samples look dark brown to black. Assuming of a direct band transition, a value of $E_g = 1.83$ eV is obtained for the $x = 0.6$ compound corresponding to an absorption edge of 678 nm. When an exponent of $\frac{1}{2}$ is used, a more realistic band gap energy of an indirect band transition in the near IR range of 1.25 eV (992 nm) is obtained. This again supports the assumption of indirect band transitions analogous to $x = 0.0$.

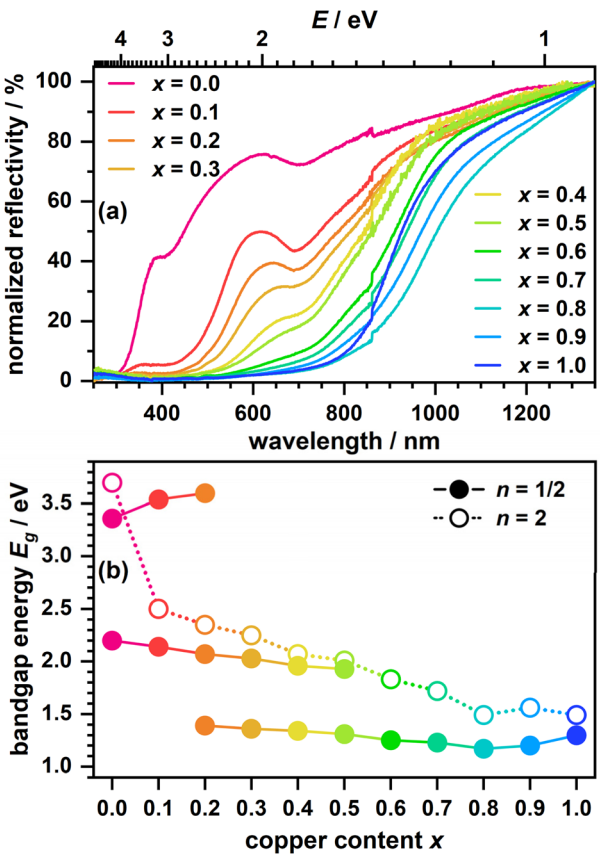

Fig. 8 (a) Normalized diffuse reflectance UV-Vis spectra for the oxyfluorides $La_2Ni_{1-x}Cu_xO_{2.5}F_3$ and (b) band gap energies E_g obtained from Kubelka–Munk transformation assuming an indirect ($n = 1/2$) as well as a direct ($n = 2$) band gap transition. The size of the symbols corresponds to the estimated error of the determination method. The step like singularity at 860 nm in (a) is an experimental artifact resulting from switching detectors.

The band structure of $La_2NiO_{2.5}F_3$ which was previously obtained applying the modified Becke–Johnson functional, revealed strong nickel d-orbital contributions to the valence band near the band gap.[16] It was therefore assumed that the insertion of one additional electron in the d-orbitals by substitution of Ni^{2+} (d^8 electron configuration) by Cu^{2+} (d^9 electron configuration) together with a strong Jahn–Teller distortion has to result in an increase in the d-orbital contribution to the valence band. To verify this assumption, DFT calculations were performed to investigate the impact of Ni/Cu-substitution on the band structure and to explain the experimentally observed change in E_g. For these calculations, a disordered Ni/Cu occupation was approximated by simulation of ordered occupations of Ni and Cu in a (110) × ($\bar{1}$10) supercell with 68-atoms (8 disordered sites). The amount of different tested configuration was highest for the low copper containing compounds with $x = 0.25$ where the strongest changes in E_g were observed in the experimental data. For each configuration the band gap was calculated using the PBEsol functional with an on-site Coulomb correction for Ni-d states. The resulting band gaps for ordered configurations were used to get an estimation of the gap of the disordered system *via* applying the generalized quasichemical approximation (GQCA).[33,34] The results for different Cu concentrations are plotted in Fig. 10a. It is observed that the general decrease of E_g with increasing x is well presented in the calculated results, although as expected the PBE (+U) method underestimated the gap of these strong correlated systems. Moreover, for most (~90%) of the configurations, the calculated band gap is indirect, and the smooth change of the calculated gap above $x = 0.75$ is consistent with the lowest E_g data obtained from the experimental measurements (Fig. 8b). Note that we used an AFM spin configuration for $x = 1$, which correctly captured the non-zero gap nature of $La_2CuO_{2.5}F_3$, while FM or non-magnetic spin-configurations result in metallic (zero gap) ground states. The band structure and DOS of $x = 0.25$ (depicted in Fig. 10b) was obtained from unfolding the supercell band structure to the unit cell k-path with the easyunfold[35] Python-package. Here the appearance of Cu-d and O-p band contribution around 1–1.5 eV within the wide bandgap of $La_2NiO_{2.5}F_3$ is confirmed and the decrease of E_g with x therefore indeed results from the additional Cu-d electrons.

The experimental E_g values in the region of the visible light makes the oxyfluorides of potential interest for the application as solar photocatalysts. First hydrogen evolution experiments were therefore performed for selected compounds with $x = 0.0$, 0.2, and 0.4 in order to test for photocatalytic hydrogen evolution reaction activity. Experiments in the presence of ethanol as

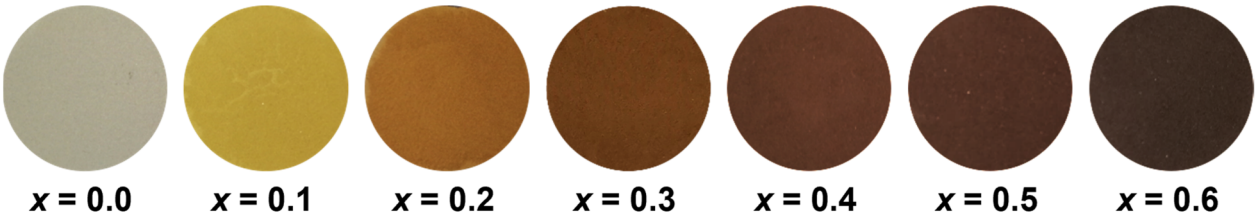

Fig. 9 Optical photographs of $La_2Ni_{1-x}Cu_xO_{2.5}F_3$ samples prepared from drying isopropanol/powder slurries on microscopy cover glasses highlighting the influence of Ni/Cu substitution of the colour of the samples.

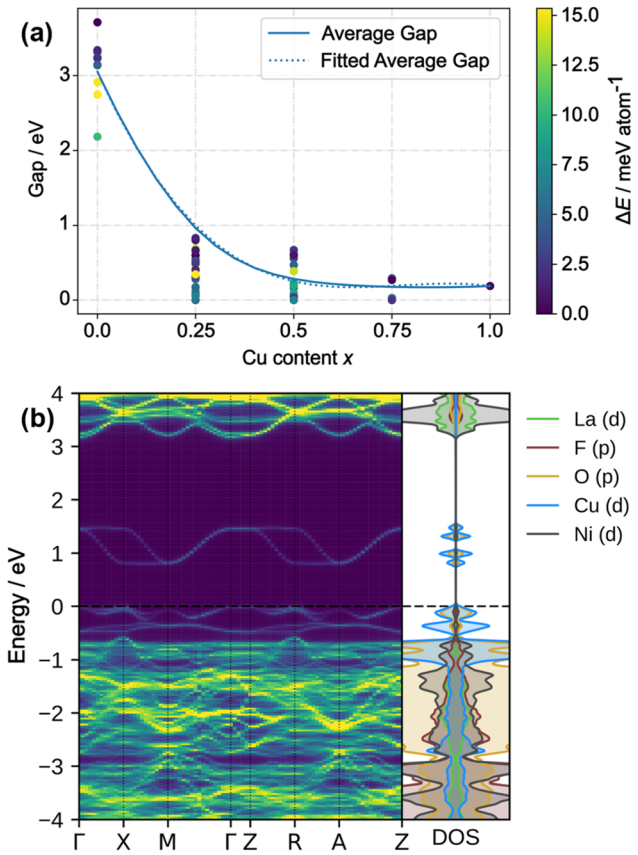

Fig. 10 (a) Band gap energy *vs.* copper content *x* data obtained from DFT calculations applying the modified Becke–Johnson functional. Data were obtained for several sample structures per *x* order to simulate a disordered Ni/Cu distribution. (b) Band structure and DOS of the $x = 0.25$ configuration obtained with the easyunfold Python package.

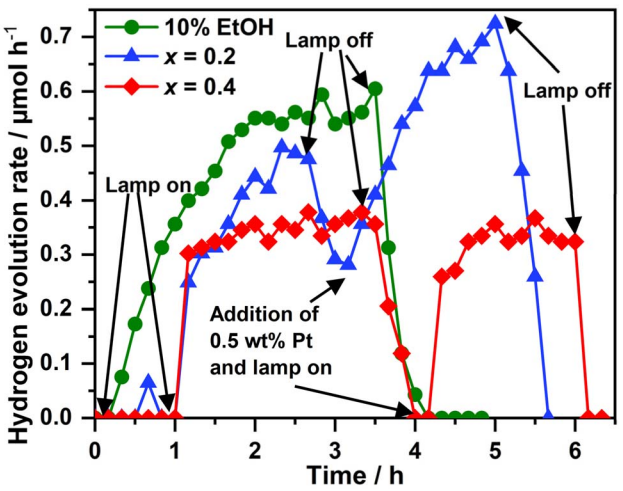

Fig. 11 Photocatalytic hydrogen evolution rate for oxyfluorides with $x = 0.2$ and 0.4 with 10% ethanol as sacrificial agent before and after addition of 0.5 wt% Pt as co-catalyst. The data of the ethanol solution without catalyst is additionally shown.

sacrificial agent were performed in two steps: 1st with the pure oxyfluoride suspension and 2nd after the addition of Pt (0.5 wt%) as co-catalyst which was photo-deposited *in situ*. The obtained H_2 evolution rates are plotted in Fig. 11 for $x = 0.2$, and 0.4 as well as the 10% ethanol solution without any catalyst. For the $x = 0.0$ sample no hydrogen was detected and the data is therefore excluded from the figure to maintain clarity. For the $x = 0.2$ and 0.4 compounds hydrogen evolution in the range of 0.3–0.45 μmol h^{-1} is obtained without the addition of Pt as cocatalyst. After the photodeposition of Pt, the hydrogen evolution increases only for the $x = 0.2$ sample to a hydrogen evolution rate of ~0.7 μmol h^{-1}. The photodeposition of Pt seems to be unsuccessful as it does not increase the hydrogen evolution rate for $x = 0.4$ and has little effect for $x = 0.2$. When comparing the amount of evolved hydrogen of the oxyfluorides with the data of the 10% ethanol solution without catalyst an increased hydrogen evolution rate is only found for the $x = 0.2$ sample. Here the maximum value of ~0.7 μmol h^{-1} after the photodeposition of Pt is slightly higher than the rate found for the pure sacrificial agent itself (~0.6 μmol l^{-1} peak activity). This highlights the necessity of pure sacrificial agent test reaction to check for the reliability of the obtained data.

The overall low amount of evolved hydrogen might be attributed to high defect concentrations in the oxyfluorides, which is indicated by reflection broadening that is observed during topochemical fluorination of the oxides with sharper diffraction peaks. Such defects might act as traps/recombination centres for the photo generated electron/hole pairs. Our aim therefore is to prepare samples with less defects for further investigations.

Conclusion

In this article, we report on the highly fluorinated Ruddlesden–Popper oxyfluorides $La_2Ni_{1-x}Cu_xO_{2.5}F_3$, which were synthesized

through a topochemical fluorination reaction of the corresponding oxides obtained from the citrate route with PVDF as fluorination agent. Single-phase samples were obtained in increments of $x = 0.1$, and a comprehensive structural study was conducted using X-ray and neutron powder diffraction data together with ^{19}F MAS NMR experiments which allowed to investigate the F environment. Our results show that the compounds up to $x = 0.9$ adopt the anion-ordered tetragonal ($P4_2/nnm$) structure of $La_2NiO_{2.5}F_3$, characterized by layer-wise alternating tilts of the Ni/CuO_4F_2 octahedra. The stability of the tetragonal structure throughout the (almost) entire substitution range is surprising, given that closely related 2F-oxyfluorides exhibit a strong symmetry reduction upon Ni^{2+} substitution by the Jahn–Teller active Cu^{2+}. In contrast, the pure cuprate endmember $La_2CuO_{2.5}F_3$ exhibits a clear symmetry reduction to triclinic $P\bar{1}$. We also characterized the optical properties of the oxyfluorides using UV-Vis measurements in combination with DFT calculations, which revealed that Ni/Cu substitution results in a Cu-d contribution to the valence band. This enables E_g to be modified across a broad range of 3.5 eV to 1.3 eV, covering the entire visible light range. Preliminary tests of the suitability of the oxyfluorides for photocatalytic hydrogen evolution showed a considerable hydrogen evolution rate for $x = 0.2$. In a follow-up article, we will discuss the impact of Ni/Cu substitution on the thermal stability, formation and decomposition reaction pathways, and magnetic properties of the title oxyfluorides $La_2Ni_{1-x}Cu_xO_{2.5}F_3$.

Author contributions

J. J.: conceptualization, data curation, formal analysis, investigation, methodology, visualization, and writing of the original draft. C. R.: collection of neutron powder diffraction data and review. K. X. and J. S. a. d. G.: collection and analysis of ^{19}F MAS NMR data and review. H.-C. W. and M. A. L. M.: performing and interpretation of theoretical calculations and review. A. H. and R. M.: performing and interpretation of photocatalytic test reactions and review. S. G. E.: resources, review, discussion and editing.

Conflicts of interest

There are no conflicts to declare.

Data availability

The data supporting the findings of this study are available within the article and its SI. The crystallographic data of all oxyfluoride has been deposited at the CCDC under deposition numbers 2471688–2471698, and can be obtained from **https://www.ccdc.cam.ac.uk/**. The neutron diffraction data are available under the following link **https://doi.ill.fr/10.5291/ILL-DATA.5-23-769**. Any other information should be requested to the corresponding authors.

Rietveld plots for the refinement of XRD data of $La_2Ni_{1-x}Cu_xO_{2.5}F_3$; Exemplarly Kubleka–Munk plots for the bandgap determination of the $x = 0.4$ compound; crystallographic data of $La_2Ni_{1-x}Cu_xO_{2.5}F_3$ obtained from Rietveld refinements. See DOI: **https://doi.org/10.1039/d5ta05605e**.

Acknowledgements

The neutron diffraction experiments was performed on the D2B diffractometer run by the Institut Laue-Langevin (ILL). Beamtime was granted under the proposal number 5-23-769 (Doi: **https://doi.ill.fr/10.5291/ILL-DATA.5-23-769**).[22] We thank the ILL for the allocated beamtime.

References

1 M. A. Nowroozi, K. Wissel, J. Rohrer, A. R. Munnangi and O. Clemens, $LaSrMnO_4$: Reversible Electrochemical Intercalation of Fluoride Ions in the Context of Fluoride Ion Batteries, *Chem. Mater.*, 2017, **29**(8), 3441–3453, DOI: **10.1021/acs.chemmater.6b05075**.

2 M. A. Nowroozi, S. Ivlev, J. Rohrer and O. Clemens, La_2CoO_4: A New Intercalation Based Cathode Material for Fluoride Ion Batteries with Improved Cycling Stability, *J. Mater. Chem. A*, 2018, **6**(11), 4658–4669, DOI: **10.1039/c7ta09427b**.

3 Y. Huang, Y. Wei, S. Cheng, L. Fan, Y. Li, J. Lin and J. Wu, Photocatalytic Property of Nitrogen-Doped Layered Perovskite $K_2La_2Ti_3O_{10}$, *Sol. Energy Mater. Sol. Cells*, 2010, **94**(5), 761–766, DOI: **10.1016/j.solmat.2009.12.020**.

4 B. Zhao, R. Wang, W. Yao, X. Yang and B. Zhou, The Effect of Copper Substitution on $La_2Ni_{1-x}Cu_xO_4$ Catalysts Activity for Simultaneous Removal of NO_x and Diesel Soot, *Catal. Lett.*, 2009, **132**(1–2), 41–49, DOI: **10.1007/s10562-009-0041-9**.

5 X. Q. Liu, J. W. Wu, X. X. Shi, H. J. Zhao, H. Y. Zhou, R. H. Qiu, W. Q. Zhang and X. M. Chen, Hybrid improper ferroelectricity in Ruddlesden-Popper $Ca_3(Ti,Mn)_2O_7$ ceramics, *Appl. Phys. Lett.*, 2015, **106**(20), 202903, DOI: **10.1063/1.4921624**.

6 Q. Zhang, A. Solanki, K. Parida, D. Giovanni, M. Li, T. L. C. Jansen, M. S. Pshenichnikov and T. C. Sum, Tunable Ferroelectricity in Ruddlesden-Popper Halide Perovskites, *ACS Appl. Mater. Interfaces*, 2019, **11**(14), 13523–13532, DOI: **10.1021/acsami.8b21579**.

7 D. Li, K. Lee, B. Y. Wang, M. Osada, S. Crossley, H. R. Lee, Y. Cui, Y. Hikita and H. Y. Hwang, Superconductivity in an Infinite-Layer Nickelate, *Nature*, 2019, **572**(7771), 624–627, DOI: **10.1038/s41586-019-1496-5**.

8 L. Si, W. Xiao, J. Kaufmann, J. M. Tomczak, Y. Lu, Z. Zhong and K. Held, Topotactic Hydrogen in Nickelate Superconductors and Akin Infinite-Layer Oxides ABO_2, *Phys. Rev. Lett.*, 2020, **124**(16), 1–8, DOI: **10.1103/PhysRevLett.124.166402**.

9 H. Sun, M. Huo, X. Hu, J. Li, Z. Liu, Y. Han, L. Tang, Z. Mao, P. Yang, B. Wang, J. Cheng, D. X. Yao, G. M. Zhang and M. Wang, Signatures of Superconductivity near 80 K in a Nickelate under High Pressure, *Nature*, 2023, **621**(7979), 493–498, DOI: **10.1038/s41586-023-06408-7**.

10 Y. Zhu, D. Peng, E. Zhang, B. Pan, X. Chen, L. Chen, H. Ren, F. Liu, Y. Hao, N. Li, Z. Xing, F. Lan, J. Han, J. Wang, D. Jia, H. Wo, Y. Gu, Y. Gu, L. Ji, W. Wang, H. Gou, Y. Shen, T. Ying,

X. Chen, W. Yang, H. Cao, C. Zheng, Q. Zeng, J. G. Guo and J. Zhao, Superconductivity in pressurized trilayer $La_4Ni_3O_{10-\delta}$ single crystals, *Nature*, 2024, **631**(8021), 531–536, DOI: 10.1038/s41586-024-07553-3.

11 R. De Barros, M. Ceretti, W. Schmidt, V. Y. Pomjakushin and W. Paulus, Growth and Oxygen Stoichiometry Control of High-Quality $La_2CoO_{4+\delta}$ Single Crystals ($\delta = 0.25$), *Cryst. Growth Des.*, 2022, **22**(9), 5542–5551, DOI: 10.1021/acs.cgd.2c00631.

12 S. Ebbinghaus, M. Fröba and A. Reller, The "Realstruktur" of the System $La_{2-x}Sr_xCu_{1-y}Ru_yO_{4-\delta}$ Studied by Rietveld and Extended X-ray Absorption Fine Structure Spectroscopy, *J. Phys. Chem. B*, 1997, **101**(48), 9909–9915, DOI: 10.1021/jp971551n.

13 P. R. Slater, Poly(vinylidene fluoride) as a reagent for the synthesis of K_2NiF_4-related inorganic oxide fluorides, *J. Fluorine Chem.*, 2002, **117**(1), 43–45, DOI: 10.1016/S0022-1139(02)00166-5.

14 J. Jacobs, A. Bivour, V. Sikolenko, H. Kohlmann, T. C. Hansen, J. R. Hester, K. Xu, J. Schmedt auf der Günne and S. G. Ebbinghaus, Unveiling the Fluorination Pathway of Ruddlesden-Popper Oxyfluorides: A Comprehensive *in Situ* X-Ray and Neutron Diffraction Study, *J. Am. Chem. Soc.*, 2025, **147**(11), 9739–9751, DOI: 10.1021/jacs.4c18187.

15 A. Bivour, J. Jacobs, F. Daumann, G. Hörner, B. Weber, C. Ritter and S. G. Ebbinghaus, Structure and Magnetic Properties of the $n = 3$ Ruddlesden-Popper Oxyfluoride $La_{0.5}Sr_{3.5}Fe_3O_{7.5}F_{2.6}$, *Inorg. Chem.*, 2024, **63**(43), 20427–20437, DOI: 10.1021/acs.inorgchem.4c02835.

16 J. Jacobs, M. A. L. Marques, H. C. Wang, E. Dieterich and S. G. Ebbinghaus, Structure, Magnetism, and Thermal Stability of $La_2NiO_{2.5}F_3$: A Ruddlesden-Popper Oxyfluoride Crystallizing in Space Group $P4_2/nnm$, *Inorg. Chem.*, 2021, **60**(17), 13646–13657, DOI: 10.1021/acs.inorgchem.1c01957.

17 S. Boumaza, R. Brahimi, L. Boudjellal, A. Belhadi and M. Trari, Photoelectrochemical study of La_2NiO_4 synthesized using citrate sol gel method—application for hydrogen photo-production, *J. Solid State Electrochem.*, 2020, **24**(2), 329–337, DOI: 10.1007/s10008-019-04470-8.

18 S. Perween, K. Wissel, Z. Dallos, M. Weiss, Y. Ikeda, S. Vasala, S. Strobel, P. Schützendübe, P. M. Jeschenko, U. Kolb, R. Marschall, B. Grabowski and P. Glatzel, Topochemical Fluorination of $LaBaInO_4$ to $LaBaInO_3F_2$, Their Optical Characterization, and Photocatalytic Activities for Hydrogen Evolution, *Inorg. Chem.*, 2023, **62**(40), 16329–16342, DOI: 10.1021/acs.inorgchem.3c01682.

19 J. Jacobs, H. C. Wang, M. A. L. Marques, K. Xu, J. Schmedt auf der Günne and S. G. Ebbinghaus, Ruddlesden-Popper Oxyfluorides $La_2Ni_{1-x}Cu_xO_3F_2$ ($0 \leq x \leq 1$): Impact of the Ni/Cu Ratio on the Structure, *Inorg. Chem.*, 2024, **63**(13), 6075–6081, DOI: 10.1021/acs.inorgchem.4c00399.

20 J. Jacobs, J. R. Hester and S. G. Ebbinghaus, Cuprate Oxyfluorides $La_2Cu_{0.8}Ni_{0.2}O_3F_2$ and $La_2CuO_3F_2$ with "Channel-like" Anion Ordering, *Inorg. Chem.*, 2022, **61**(43), 17202–17211, DOI: 10.1021/acs.inorgchem.2c02776.

21 J. Jacobs, H. C. Wang, M. A. L. Marques and S. G. Ebbinghaus, Ruddlesden-Popper Oxyfluorides $La_2Ni_{1-x}Cu_xO_3F_2$ ($0 \leq x \leq 1$): Impact of the Ni/Cu Ratio on the Thermal Stability and Magnetic Properties, *Inorg. Chem.*, 2024, **63**(24), 11317–11324, DOI: 10.1021/acs.inorgchem.4c01330.

22 J. Jacobs, A. Bivour, S. G. Ebbinghaus and C. Ritter, *Solving the Structure of New $n = 1$ and $n = 3$ Ruddlesden–Popper Oxyfluorides with Unique Structural Distortions by High Resolution Neutron Powder Diffraction*, 2021, DOI: 10.5291/ILL-DATA.5-23-769.

23 B. H. Toby and R. B. Von Dreele, GSAS-II: The Genesis of a Modern Open-Source All Purpose Crystallography Software Package, *J. Appl. Crystallogr.*, 2013, **46**(2), 544–549, DOI: 10.1107/S0021889813003531.

24 K. Xu, F. Aldudak, O. Pecher, M. Braun, A. Neuberger, H. Foysi and J. Schmedt auf der Günne, High resolution solid-state NMR on the desktop, *Solid State Nucl. Magn. Reson.*, 2023, **126**, 101884, DOI: 10.1016/j.ssnmr.2023.101884.

25 R. K. Harris, E. D. Becker, S. M. C. De Menezes, R. Goodfellow and P. Granger, NMR Nomenclature: Nuclear Spin Properties and Conventions for Chemical Shifts - IUPAC Recommendations 2001, *Solid State Nucl. Magn. Reson.*, 2002, **22**(4), 458–483, DOI: 10.1006/snmr.2002.0063.

26 D. Jardón-Álvarez and J. Schmedt auf der Günne, Reduction of the Temperature Gradients in Laser Assisted High Temperature MAS NMR, *Solid State Nucl. Magn. Reson.*, 2018, **94**, 26–30, DOI: 10.1016/j.ssnmr.2018.08.002.

27 D. Joubert, From Ultrasoft Pseudopotentials to the Projector Augmented-Wave Method, *Phys. Rev. B:Condens. Matter Mater. Phys.*, 1999, **59**(3), 1758–1775, DOI: 10.1103/PhysRevB.59.1758.

28 G. Kresse and J. Furthmüller, Efficiency of *Ab Initio* Total Energy Calculations for Metals and Semiconductors Using a Plane-Wave Basis Set, *Comput. Mater. Sci.*, 1996, **6**(1), 15–50, DOI: 10.1016/0927-0256(96)00008-0.

29 G. Kresse and J. Furthmüller, Efficient Iterative Schemes for *Ab Initio* Total-Energy Calculations Using a Plane-Wave Basis Set, *Phys. Rev. B*, 1996, **54**(16), 11169–11186, DOI: 10.1103/PhysRevB.54.11169.

30 J. P. Perdew, K. Burke and M. Ernzerhof, Generalized Gradient Approximation Made Simple, *Phys. Rev. Lett.*, 1996, **77**(18), 3865–3868, DOI: 10.1103/PhysRevLett.77.3865.

31 S. Dudarev and G. Botton, Electron-Energy-Loss Spectra and the Structural Stability of Nickel Oxide: An LSDA+U Study, *Phys. Rev. B*, 1998, **57**(3), 1505–1509, DOI: 10.1103/PhysRevB.57.1505.

32 A. van de Walle, Multicomponent multisublattice Alloys, nonconfigurational entropy and other additions to the Alloy Theoretic Automated Toolkit, *CALPHAD:Comput. Coupling Phase Diagrams Thermochem.*, 2009, **33**(2), 266–278, DOI: 10.1016/j.calphad.2008.12.005.

33 A. Sher, M. Van Schilfgaarde, A. B. Chen and W. Chen, Quasichemical Approximation in Binary Alloys, *Phys. Rev. B*, 1987, **36**(8), 4279–4295, DOI: 10.1103/PhysRevB.36.4279.

34 L. Teles, J. Furthmüller, L. Scolfaro, J. Leite and F. Bechstedt, First-Principles Calculations of the Thermodynamic and Structural Properties of Strained and Alloys, *Phys. Rev. B*, 2000, **62**(4), 2475–2485, DOI: **10.1103/PhysRevB.62.2475**.

35 B. Zhu, S. R. Kavanagh and D. Scanlon, Easyunfold: A Python Package for Unfolding Electronic Band Structures, *J. Open Source Softw.*, 2024, **9**(93), 5974, DOI: **10.21105/joss.05974**.

36 O. Clemens and P. R. Slater, Topochemical modifications of mixed metal oxide compounds by low-temperature fluorination routes, *Rev. Inorg. Chem.*, 2013, **33**(2–3), 105–117, DOI: **10.1515/revic-2013-0002**.

37 A. Aguadero, J. A. Alonso, M. J. Escudero and L. Daza, Evaluation of the $La_2Ni_{1-x}Cu_xO_{4+\delta}$ System as SOFC Cathode Material with 8YSZ and LSGM as Electrolytes, *Solid State Ionics*, 2008, **179**(11–12), 393–400, DOI: **10.1016/j.ssi.2008.01.099**.

38 P. Makuła, M. Pacia and W. Macyk, How To Correctly Determine the Band Gap Energy of Modified Semiconductor Photocatalysts Based on UV-Vis Spectra, *J. Phys. Chem. Lett.*, 2018, **6**, 6814–6817, DOI: **10.1021/acs.jpclett.8b02892**.